Journal of
Marine Science and Engineering

MDPI

Article

Research on a DC–DC Converter and Its Advanced Control Strategy Applied to the Integrated Energy System of Marine Breeding Platforms

Hongxing Chen [1], Weiming Lin [2] and Wei He [1,*]

[1] Fujian Engineering Research Center of Safety Control for Ship Intelligent Navigation, College of Physics and Electronic Information Engineering, Minjiang University, Fuzhou 350108, China
[2] Fujian Key Laboratory of New Energy Generation and Power Conversion, Fuzhou University, Fuzhou 350108, China
* Correspondence: hewei11@mju.edu.cn; Tel.: +86-186-0699-0698

Abstract: The deep-sea aquaculture industry will become one of the important pillars of the future marine economy. However, the application of clean energy in the new scenario needs to be strengthened for platform operation. For this kind of renewable-energy distributed-generation system, an energy storage system is essential. A bidirectional DC–DC converter is essential for distributed power generation systems. It connects a variety of renewable energy sources with energy storage cells. A high-gain bidirectional Cuk circuit with zero ripple is proposed in the paper. It is characterized by a simple structure, zero ripple, low voltage stress of semiconductor power devices, and high voltage gain. A passivity-based control with linear active disturbance rejection is proposed to solve the problems of the large steady-state error. The zero steady-state error, strong robustness, and whole-range stability have been obtained for the proposed control strategy. Finally, a simulation was carried out. A 100 W, 48 V/400 V prototype was built to verify the validity of the theoretical analysis for the proposed circuit. The improved passivity-based control strategy was verified to solve the contradiction between rapidity and overshoot. It can be realized to improve the dynamic performance of the proposed converter and achieve robust control.

Keywords: deep-sea aquaculture industry; integrated energy system; bidirectional DC–DC Cuk converter; high voltage gain; switched capacitor cell; passivity-based control; linear active disturbance rejection

Citation: Chen, H.; Lin, W.; He, W. Research on a DC–DC Converter and Its Advanced Control Strategy Applied to the Integrated Energy System of Marine Breeding Platforms. *J. Mar. Sci. Eng.* **2023**, *11*, 512. https://doi.org/10.3390/jmse11030512

Academic Editors: Wei-Hsin Chen, Aristotle T. Ubando, Chih-Che Chueh and Liwen Jin

Received: 20 January 2023
Revised: 20 February 2023
Accepted: 22 February 2023
Published: 27 February 2023

1. Introduction

The ocean is known as the “blue granary”. Most of the traditional marine fisheries are extensive aquaculture in bays or shallow beaches. Now, with the rapid development of marine fisheries, the aquaculture mode has changed from “light blue” to “deep blue” [1]. The profound marine aquaculture industry will become one of the important pillars of the future marine economy. However, most of the existing deep-water aquaculture platforms only use fuel engines as energy devices, with high noise, many pollutants, and amplified harmful gas emissions. Moreover, with the development of the deep-sea and offshore aquaculture industry, the energy required for platform operation is growing continuously, and the consumption of traditional fossil energy is huge. The massive use of oil will lead to marine environmental pollution, restricting its sustainable development [2]. Therefore, attention should be given to the development and utilization of clean energy such as solar energy and wind energy. The integrated energy system of an aquaculture platform is subject to the intermittent strong impact of clean energy, which easily causes untimely energy regulation and unsafe offshore production. The safe, efficient, and green integrated energy utilization of aquaculture platforms is facing new theoretical and technical challenges [3].

The development of distributed power generation systems is a resolution to mitigate high fossil-fuel dependency, especially in the deep-sea aquaculture industry where the possibility of grid connection is still uncertain. Most of them are heavily dependent on transported fossil fuels. Therefore, installing a distributed power generation system for these aquaculture industries is seen as very promising. The distributed power generation system and its power conversion are interrelated systems. A suitable power converter system is designed based on the output voltage or current amplitude at the generator side and to match the conditions at the load. This process ensures a smooth power transfer from generator side to the loads. Among them, a bidirectional DC–DC converter is essential for distributed power-generation systems. It connects the bus terminal with energy storage cells such as batteries or supercapacitors, and realizes the management and rational utilization of system energy [4,5].

For renewable-energy power-generation systems on deep-sea aquaculture platforms, a DC microgrid mode is often used because of its simple structure, no phase synchronization, reactive power loss, and harmonics [6]. Additionally, the DC bus voltage is usually high. However, the output voltage of batteries is usually low. An additional battery equalization circuit is required if the output port voltage is increased by the battery series. It increases unnecessary costs and reduces system reliability. In addition, the load of the breeding platform includes the mixer, feeder, household electricity, and so on. These devices start and stop frequently with different needs in the process of breeding. It causes the power load to fluctuate constantly. Hence, the bidirectional converters require high voltage gain and high efficiency. Advanced control strategy is indispensable, which makes the system maintain stable and fast dynamic response. However, there are few high-gain bidirectional converters and their advanced control strategies are necessary in the marine field. This paper is a good supplement to the research gap and needs.

In recent years, to improve the voltage gain and the conversion efficiency of the converter, some bidirectional high-gain DC–DC converters have been proposed. For example, [7] proposes a quadratic bidirectional buck/boost circuit with the same gain as the basic cascade type. However, there are many semiconductor devices in this circuit, and the voltage stress of semiconductor devices is large on the high-voltage side. As described in [8], cascading different bidirectional converters by multiplexing the switching tubes increases the gain and reduces the number of switches, but switching the circuit causes high voltage stress on the output side. In addition, networks such as switched capacitors [9], switched inductors [10], coupled inductors [11,12], and Z-sources [13] are introduced to increase the range in voltage gain for the converter. Among them, a family of pure switched-capacitor, bidirectional high-gain DC–DC circuits is proposed in [9]. It can enable higher power density due to the absence of magnetic components. However, its output voltage can only be an integer multiple of the input voltage, and there is a current spike on the capacitor. Based on a bidirectional DC–DC circuit, a switching inductor unit is introduced [10], which limits the current spikes of the pure switched capacitor. However, the voltage stress of switching is large on the high-voltage side. To increase the voltage gain, a composite nonisolated, bidirectional buck/boost circuit is proposed by multiplexing the inductor as the primary winding of the flyback converter [11]. However, the current waveform of this topology is a square wave on the low-voltage side, and the current ripple on the low-voltage side is large. Accordingly, the tapped inductor is introduced into bidirectional quadratic DC–DC converters to improve the converter gain and reduce the current ripple on the low-voltage side [12], but there is also the problem of the large voltage stress of the switching on the high-voltage side. In addition, [13] introduces a Z-source network into the bidirectional buck/boost converter, improving the voltage-gain range and reliability of the converter. However, it increases the current stress of the main switch. These studies are mainly concentrated on systems connected to a large power grid. However, owing to the particularity of the marine environment, current research on high-gain bidirectional circuits is minimal.

In addition, because load variations and external disturbances are often uncertain and fluctuating in the marine environment, the traditional control strategy cannot guarantee the dynamic response of the system over a wide range of input and load variations, as well as making it difficult to further improve system performance. Passive-based control was successfully applied to DC–DC converters, as described in [14]. This scheme is a globally stable control strategy with simple implementation and strong robustness. However, there are steady-state output errors. The amount of injection damping affects the effectiveness of the control and there is no single design method for optimal damping. To analyze the effect of injection damping, the range of injection damping was analyzed and a genetic algorithm was used to find the optimal injection damping [15], but the calculation process is complicated. To reduce the steady-state output error, the parasitic resistance of the device and the on-state voltage drop of the semiconductor device are considered in the modeling process [16]. However, it is not conducive to real-time control due to its computational complexity. A novel passive-based control is proposed by combining it with PI control [17]. Zero steady-state error was achieved by obtaining the current reference through the voltage outer loop, but there is an irreconcilable conflict between rapidity and overshoot. In addition, the proposed control strategy described in [18] reduces the jitter under sliding mode control and suppresses the voltage overshoot under passive-based control by combining sliding mode control with passive control. However, there are still steady-state errors, narrow-amplitude vibration, and a large output ripple in this control. A passivity-based control strategy with a nonlinear disturbance observer is proposed in [19], where the effects of parameter uncertainty and system disturbances are compensated by a nonlinear disturbance observer. It reduces the steady-state error under typical passive control and improves the control robustness of the system, but the implementation of the existing observer is more complicated. Moreover, IDA-PBC has been proposed in [20] as a control technique for designing high-performance nonlinear controllers for systems described by port-Hamiltonian models. This method achieves stabilization by rendering the system passive with respect to a desired storage function and injecting damping. The development of IDA-PBC control law via modification in interconnection and damping matrices for the rectifier is discussed in [21,22].

In the marine environment, the current research on high-gain bidirectional circuits and their control strategy is minimal. A bidirectional high-gain Cuk converter with zero-ripple is proposed in this paper. It uses switched-capacitor gain units to increase the voltage gain range. The EL model of the proposed converter is developed from the global energy perspective based on the dynamic modeling method. Then, based on this EL model, passivity-based control with linear active disturbance rejection is proposed to solve the problem of large steady-state errors that are caused by model errors and disturbances in the bidirectional high-gain converter using typical passivity-based control. The control strategy is characterized by strong robustness and global stability. Afterward, the proposed converter and control strategy are specifically analyzed in the paper, and the voltage gain relationship, ripple characteristics, and voltage stress characteristics are analyzed in detail. Finally, the important parameters of the proposed converter and control strategy are designed and analyzed in this paper. As described herein, a simulation was carried out and a 100W, 48V/400V prototype was built to verify the validity of the theoretical analysis of the proposed circuit. The simulation and experimental results show that the proposed circuit achieves high voltage gain, low voltage stress, and zero ripple. The proposed control method improves the dynamic performance of the converter and achieves robust control and zero steady-state error.

The remainder of this paper is organized as follows. Section 2 provides the proposed converter's operation process and principle. In Section 3, the improved control strategy is formulated. The simulation and experimental results are presented in Section 4. Discussion is provided in Section 5. Finally, Section 6 concludes this paper.

2. Bidirectional High-Gain Cuk Converter

2.1. Topology of Circuit

By combining basic a bidirectional Cuk circuit with a gain cell, a bidirectional high-gain Cuk converter with zero ripple is proposed in this paper. The basic bidirectional Cuk is shown in Figure 1, and the proposed converter is shown in Figure 2. The circuit consists of V_1, V_2, L_1, L_2, S_{B1}, S_{B2}, C_B, and the gain network of C_{2n-1}, C_{2n}, S_{2n-1}, and S_{2n}, where the diodes D_{B1}, D_{B2}, D_1, ..., D_{2n} are parasitic body diodes corresponding to power switching.

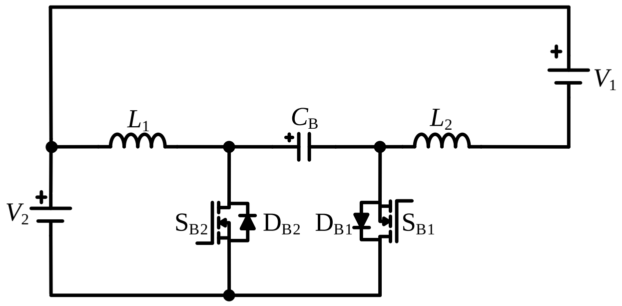

Figure 1. Basic bidirectional Cuk converter.

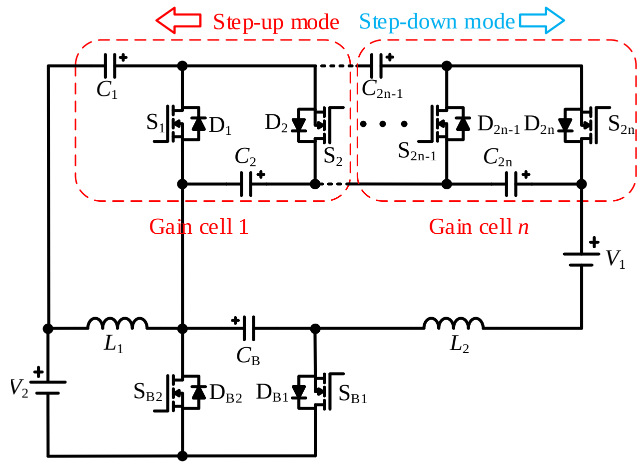

Figure 2. A scalable high-gain bidirectional Cuk converter with zero ripple.

2.2. Operating Principle of the Converter

We take the bidirectional high-gain Cuk circuit with a basic gain network as an example to illustrate the operating principle and operating process for the proposed converter, and its equivalent circuit in step-up/step-down mode is shown in Figures 3 and 4. The proposed circuit operates with V_1 as the high-voltage side and V_2 as the low-voltage side. This circuit exists in two electrical energy conversion directions, such as step-up direction conversion and step-down direction conversion. When the converter works in the step-up mode, the low-voltage side provides energy to the high-voltage side, and S_{B2}, D_{B1}, D_1, and D_2 are in working condition. When the converter works in the step-down mode, the high-voltage side provides energy to the low-voltage side, and S_{B1}, S_1, S_2, and D_{B2} are in working condition.

To simplify the analysis, the following assumptions are made: (1) the voltage across the capacitor is constant at steady state; (2) all devices are ideal devices and the effect of parasitic parameters is not considered; (3) the circuit operates in CCM mode.

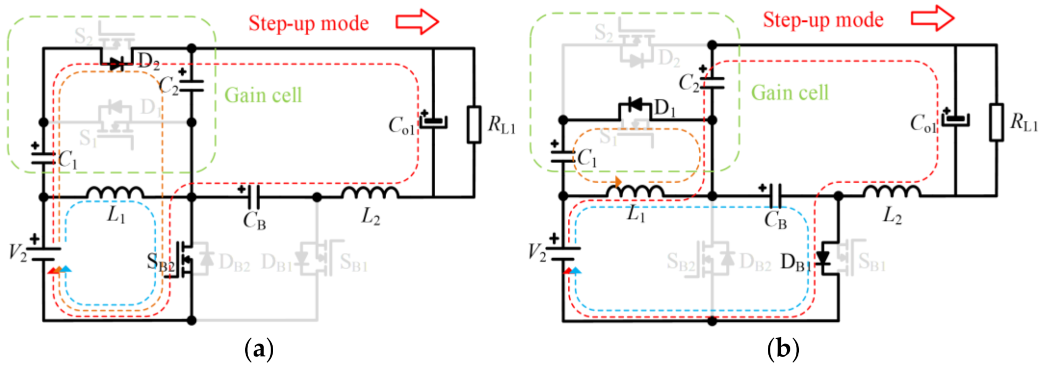

Figure 3. The equivalent circuit of the operation modes in step-up mode: (**a**) S_{B2} on; (**b**) S_{B2} off.

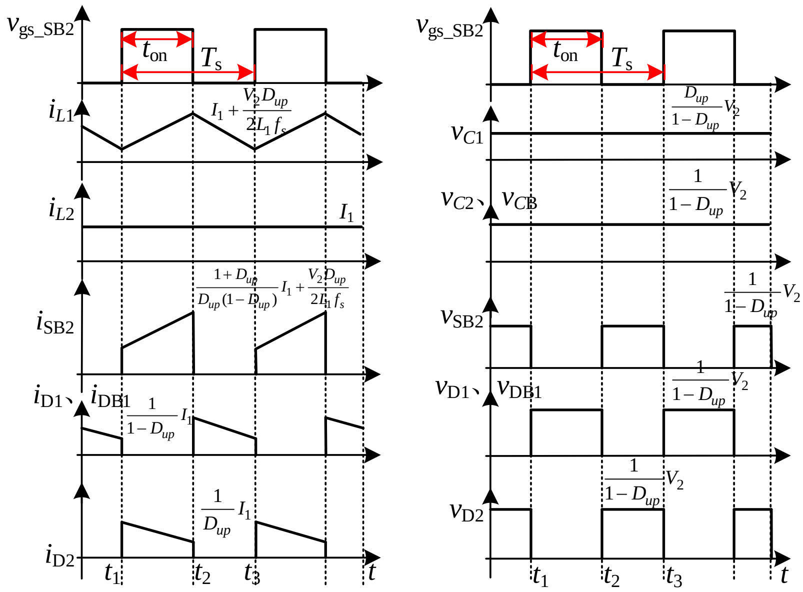

Figure 4. The operation waveforms of main components in step-up mode.

2.2.1. Step-Up Mode

At steady state, there are two operating stages in one duty cycle. The equivalent circuit of each switching stage and its main operating waveforms are shown in Figures 3 and 4, where v_{gs_SB2} is the drive signal for S_{B2}. As shown in the figures, i_{L1}, i_{L2} is the current flowing through inductor L_1, L_2; i_{C1}, i_{C2}, i_{CB} is the current flowing through capacitor C_1, C_2, C_B; i_{SB2}, i_{D1}, i_{D2}, i_{DB1} is the current flowing through S_{B2}, D_1, D_2, D_{B1}; and T_s is a switching cycle. The operating process of the circuit is as follows.

Mode 1 (t_1–t_2): The equivalent operating circuit in this stage is shown in Figure 3a. At the moment of t_1, S_{B2} and D_2 are turned on, diodes D_1 and D_{B1} are turned off. The low-voltage side charges inductor L_1. Capacitor C_1 and low-voltage side charges C_2, and the low-voltage side, capacitor C_1, and capacitor C_B are connected in series to charge inductor L_2 and supply the high-voltage side. The inductor current reaches its maximum value until moment t_2. In this mode, the voltage and current of the inductor L_1 are:

$$\begin{cases} v_{L1\_1} = V_2 = V_{C2} - V_{C1} \\ i_{L1\_1}(t) = I_2 - \frac{v_{L1\_1} D_{up}}{2L_1 f_s} + \frac{v_{L1\_1}}{L_1} t \\ \Delta i_{L1\_1} = \frac{v_{L1\_1} D_{up}}{L_1 f_s} \end{cases} \quad (1)$$

The voltage and current of inductor L_2 are:

$$\begin{cases} v_{L2\_1} = V_{C2} + V_{CB} - V_1 \\ i_{L2\_1}(t) = I_1 - \frac{v_{L2\_1} D_{up}}{2L_2 f_s} + \frac{v_{L2\_1}}{L_2} t \\ \Delta i_{L2\_1} = \frac{v_{L2\_1} D_{up}}{L_1 f_s} \end{cases} \quad (2)$$

where I_2 and I_1 are the average values of the input current on the low-voltage side and the output current on the high-voltage side, respectively. V_{C1} is the voltage across capacitor C_1, V_{C2} is the voltage across capacitor C_2, and V_{CB} is the voltage across capacitor C_B.

Mode 2 (t_2–t_3): The equivalent operating circuit in this stage is shown in Figure 3b. At the moment of t_2, S_{B2} and D_2 are turned off, diodes D_1 and D_{B1} are turned on. Inductor L_1 charges capacitor C_1. The low-voltage side and inductor L_1 charge C_B. The low-voltage side, inductor L_1, and capacitor C_2 are connected in series to supply the high-voltage side. In this mode, the voltage and current of the inductor L_1 are:

$$\begin{cases} v_{L1\_2} = V_2 - V_{CB} = -V_{C1} \\ i_{L1\_2}(t) = I_2 - \frac{v_{L1\_2}(1-D_{up})}{2L_1 f_s} + \frac{v_{L1\_2}}{L_1}(t - D_{up} T_s) \\ \Delta i_{L1\_2} = \frac{v_{L1\_2}(1-D_{up})}{L_1 f_s} \end{cases} \quad (3)$$

The voltage and current of the inductor L_2 are:

$$\begin{cases} v_{L2\_2} = V_2 + V_{C1} + V_{CB} - V_1 = V_{C2} + V_{CB} - V_1 \\ i_{L2\_2}(t) = I_1 - \frac{v_{L2\_2}(1-D_{up})}{2L_2 f_s} + \frac{v_{L2\_2}}{L_2}(t - D_{up} T_s) \\ \Delta i_{L2\_2} = \frac{v_{L2\_1}(1-D_{up})}{L_1 f_s} \end{cases} \quad (4)$$

The inductor current reaches its minimum value until moment t_3. This stage ends when the switching S_{B2} turns on at moment t_3.

2.2.2. Step-Down Mode

At steady state, there are two operating stages in one duty cycle. The equivalent circuit of each switching stage and its main operating waveforms are shown in Figures 5 and 6, where v_{gs_SB1} is the drive signal for S_{B1}, v_{gs_S1} is the drive signal for S_{B1}, and v_{gs_S2} is the drive signal for S_2. As shown in the figures, i_{L1}, i_{L2} is the current flowing through inductor L_1, L_2; i_{C1}, i_{C2}, i_{CB} is the current flowing through capacitor C_1, C_2, C_B; i_{SB2}, i_{D1}, i_{D2}, i_{DB1} is the current flowing through S_{B2}, D_1, D_2, D_{B1}; and T_s is a switching cycle. The operating process of the circuit is as follows.

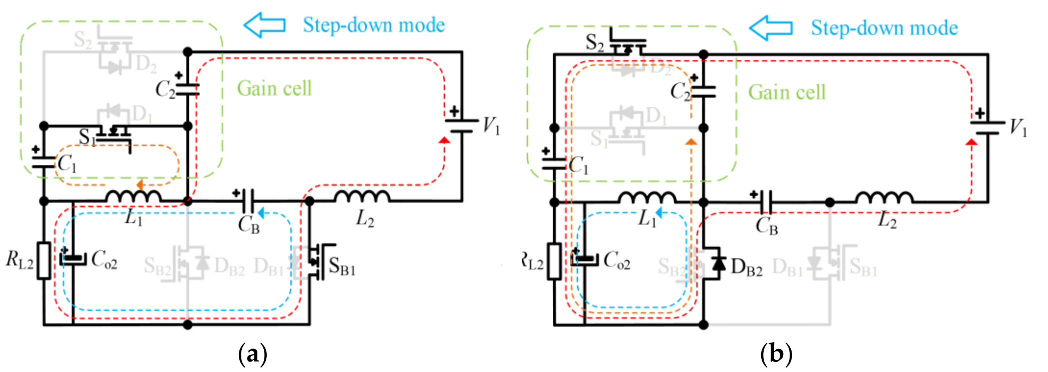

Figure 5. The equivalent circuit of the operation modes in step-down mode: (**a**) S_{B1} S_1 on, S_2 off; (**b**) S_2 on, S_{B1} S_1 off.

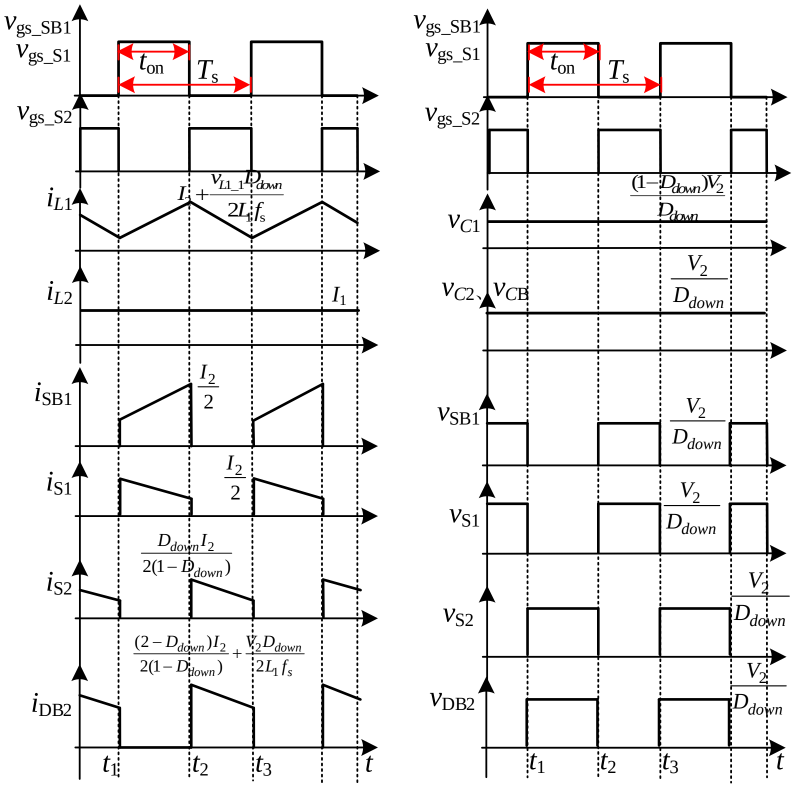

Figure 6. The operation waveforms of main components in step-down mode.

Mode 1 (t_1–t_2): The equivalent operating circuit in this stage is shown in Figure 5a. At the moment of t_1, S_2 and D_{B1} are turned on, capacitor C_1 charges inductor L_1. The high-voltage side V_1 charges capacitor C_2, L_1, L_2 and the low-voltage side. Capacitor C_B supplies the low-voltage side and L_1. The inductor current reaches its maximum value until moment t_2. In this mode, the voltage and current of the inductor L_1 are:

$$\begin{cases} v_{L1\_1} = V_{C1} = V_{CB} - V_2 \\ i_{L1\_1}(t) = I_2 - \frac{v_{L1\_1} D_{down}}{2L_1 f_s} + \frac{v_{L1\_1}}{L_1} t \\ \Delta i_{L1\_2} = \frac{v_{L1\_1} D_{down}}{L_1 f_s} \end{cases} \tag{5}$$

The voltage and current of the inductor L_2 are:

$$\begin{cases} v_{L2\_1} = V_1 - V_{C2} - V_{CB} \\ i_{L2\_1}(t) = I_1 - \frac{v_{L2\_1} D_{down}}{2L_2 f_s} + \frac{v_{L2\_1}}{L_2} t \\ \Delta i_{L2\_1} = \frac{v_{L2\_1} D_{down}}{L_2 f_s} \end{cases} \tag{6}$$

Mode 2 (t_2–t_3): The equivalent operating circuit in this stage is shown in Figure 5b. At the moment of t_2, S_{B1} and S_1 are turned off, S_2 and D_{B1} are turned on. Inductor L_1 charges the low-voltage side. Capacitor C_2 charges C_1 and the low-voltage side. The high-voltage side V_1 charges capacitor C_1, C_B, and the low-voltage side. In this mode, the voltage and current of the inductor L_1 are:

$$\begin{cases} v_{L1\_2} = -V_2 = V_{C1} - V_{C2} \\ i_{L1\_2}(t) = I_2 + \frac{v_{L1\_2} D_{down}}{2L_1 f_s} + \frac{v_{L1\_2}}{L_1}(t - D_{down} T_s) \\ \Delta i_{L1\_2} = \frac{v_{L1\_2} D_{down}}{L_1 f_s} \end{cases} \tag{7}$$

The voltage and current of the inductor L_2 are:

$$\begin{cases} v_{L2\_2} = V_1 - (V_2 + V_{\text{C1}} + V_{\text{CB}}) = V_1 - V_{\text{C2}} - V_{\text{CB1}} \\ i_{L2\_2}(t) = I_1 + \frac{v_{L2\_2} D_{down}}{2L_2 f_\text{s}} + \frac{v_{L2\_2}}{L_2}(t - D_{down} T_\text{s}) \\ \Delta i_{L2\_2} = \frac{v_{L2\_2} D_{down}}{L_2 f_\text{s}} \end{cases} \tag{8}$$

The inductor current reaches its minimum value until moment t_3. This stage ends when the switching S_{B1} and S_1 turns on at moment t_3.

2.3. Steady-State Characterization

2.3.1. Voltage Gain

1. Step-up mode

At steady state, the inductance characteristics of the proposed converter satisfy the volt–second balance relation, and the average value of the intermediate capacitance–voltage can be obtained from Equations (1) and (3).

$$\begin{cases} V_{C1} = \frac{D_{up}}{1 - D_{up}} V_2 \\ V_{C2} = \frac{1}{1 - D_{up}} V_2 \\ V_{CB} = \frac{1}{1 - D_{up}} V_2 \\ V_1 = V_{C2} + V_{CB} = \frac{2}{1 - D_{up}} V_2 \end{cases} \tag{9}$$

The voltage gain of the bidirectional high-gain Cuk circuit with the basic gain network in step-up mode is:

$$M_{up} = \frac{V_1}{V_2} = \frac{2}{1 - D_{up}} \tag{10}$$

Similarly, by analyzing the operating principle of the bidirectional high-gain Cuk circuit with multigain network, we can obtain the voltage gain in step-up mode as follows.

$$M_{up} = \frac{V_1}{V_2} = \frac{1 + n}{1 - D_{up}} \tag{11}$$

where n is the number of gain cells.

2. Step-down mode

Similarly, by analyzing the operating principle, we can obtain the voltage gain of bidirectional high-gain Cuk circuit with basic gain network in step-down mode as follows.

$$M_{down} = \frac{V_2}{V_1} = \frac{D_{down}}{2} \tag{12}$$

The voltage gain of bidirectional high-gain Cuk circuit with multigain network in step-down mode:

$$M_{down} = \frac{V_2}{V_1} = \frac{D_{down}}{1 + n} \tag{13}$$

2.3.2. Zero Ripple Characteristics

1. Step-up mode

At steady state, the inductance characteristics of L_2 in step-up mode satisfy the volt–second balance relation. It is also known that the voltage across inductor L_2 in one switching cycle is the same from Equations (2) and (4). The voltage of L_2 is:

$$\begin{aligned} v_{L2\_1} &= v_{L2\_2} = V_{C2} + V_{CB} - V_1 \\ &= \frac{1}{1 - D_{up}} V_2 + \frac{1}{1 - D_{up}} V_2 - \frac{2}{1 - D_{up}} V_2 = 0 \end{aligned} \tag{14}$$

Therefore, the voltage across the inductor L_2 is constantly zero, and it is known that the instantaneous the current of L_2 is:

$$i_{L2}(t) = I_1 \tag{15}$$

Therefore, the proposed converter achieves zero current ripple on the high-voltage side.

2. Step-down mode

Similarly, analyzing the operating principle, the proposed converter achieves zero current ripple on the high-voltage side.

2.3.3. Voltage Stress of the Power Device

1. Step-up mode

Analyzing the operation of the converter, the voltage stress of S_{B2} is:

$$v_{\mathrm{SB2\_max}} = V_{CB} = \frac{1}{1 - D_{up}} V_2 = \frac{V_1}{2} \tag{16}$$

The voltage stress of D_1, D_2, and D_{B1} is:

$$v_{\mathrm{D1.max}} = v_{\mathrm{D2.max}} = v_{\mathrm{DB1.max}} = \frac{1}{1 - D_{up}} V_2 = \frac{V_1}{2} \tag{17}$$

Similarly, at the step-up mode, the voltage stress of all power devices in the bidirectional high-gain Cuk circuit with multigain network is:

$$v_{S.\mathrm{max}} = \frac{V_1}{1+n} \tag{18}$$

2. Step-down mode

The voltage stress of S_1, S_2, and S_{B1} is:

$$v_{\mathrm{S1.max}} = v_{\mathrm{S2.max}} = v_{\mathrm{SB1\_max}} = \frac{1}{D_{down}} V_2 = \frac{V_1}{2} \tag{19}$$

The voltage stress of D_{B2} is:

$$v_{\mathrm{DB2\_max}} = V_{CB} = \frac{1}{D_{down}} V_2 \tag{20}$$

Similarly, at the step-down mode, the voltage stress of all power devices in the bidirectional high-gain Cuk circuit with multigain network is:

$$v_{S.\mathrm{max}} = \frac{V_1}{1+n} \tag{21}$$

2.3.4. Characteristic Comparison

The characteristic comparison of the proposed converter with the counterparts is shown in Table 1. The conventional buck/boost converter can achieve bidirectional power flows while employing the fewest number of power switches, but the converter's conversion ratio range is limited. The converter in reference [12] has a high step-up/step-down conversion ratio, but the voltage stress is high. Compared with the converters in reference [12], the converter's voltage stress in reference [23] has been improved, but the converter's conversion ratio range is limited. It can be seen that the proposed converter achieves a high and wide voltage-gain range. The voltage stress is reduced further, and the ripple is low.

Table 1. Characteristic comparison of the proposed converter with its main competitors.

Bidirectional Converter	Max. Voltage Stress of Switches	Efficiency	Structural Complexity	N_S	Ripple	Voltage Gain Step-Up	Voltage Gain Step-Down
Buck/Boost Converter	V_H	-	simple	2	large	$\frac{1}{1-D}$	D
Converter described in [23]	V_H	88.9~92.3% (250 W)	complex	4	large	$\frac{1}{(1-D)^2}$	D^2
Converter in [24] (one-cell)	$\frac{V_L+V_H}{2}$	-	complex	3	low	$\frac{1+D}{1-D}$	$\frac{D}{2-D}$
Proposed Converter	$\frac{1}{1+n} \cdot V_H$	91.5~94.8% (100 W, two-cell)	complex	4	low	$\frac{1+n}{1-D}$	$\frac{D}{1+n}$

3. Passivity-Based Control with LADRC

For the converter shown in Figure 2, the Euler–Lagrange equations are used to build the EL model of the bidirectional high-gain Cuk circuit [24]. The inductive charge and capacitive charge in the circuit are chosen as the generalized coordinates $\boldsymbol{q}$ of the proposed converter. Thus, the kinetic energy $K(\dot{\boldsymbol{q}}, \boldsymbol{q})$, potential energy $G(\boldsymbol{q})$, and dissipation function $W(\dot{\boldsymbol{q}})$ of the circuit are obtained, and the external force $\boldsymbol{F}_q$ for each energy component is obtained. Then, the EL equation of the circuit can be obtained [25]:

$$\begin{cases} E(\dot{\boldsymbol{q}}, \boldsymbol{q}) = K(\dot{\boldsymbol{q}}, \boldsymbol{q}) - G(\boldsymbol{q}) \\ \frac{\mathrm{d}}{\mathrm{d}t}\left(\frac{\partial E(\dot{\boldsymbol{q}}, \boldsymbol{q})}{\partial \dot{\boldsymbol{q}}}\right) - \frac{\partial E(\dot{\boldsymbol{q}}, \boldsymbol{q})}{\partial \boldsymbol{q}} + \frac{\partial W(\dot{\boldsymbol{q}})}{\partial \dot{\boldsymbol{q}}} = \boldsymbol{F}_q \end{cases} \tag{22}$$

Using the switching function $\mu(t)$, the EL equation for each stage is obtained as follows.

$$\boldsymbol{D}_B \cdot \dot{\boldsymbol{x}} + \boldsymbol{J}_B \cdot \boldsymbol{x} + \boldsymbol{R}_B \cdot \boldsymbol{x} = \boldsymbol{F} \tag{23}$$

The respective matrices in step-up mode are:

$$\begin{aligned} \boldsymbol{J}_B &= \begin{bmatrix} 0 & 0 & 1 & -\mu(t) & 0 & 0 \\ 0 & 0 & 0 & -1 & -1 & 1 \\ -1 & 0 & 0 & 0 & 0 & 0 \\ \mu(t) & 1 & 0 & 0 & 0 & 0 \\ 0 & 1 & 0 & 0 & 0 & 0 \\ 0 & -1 & 0 & 0 & 0 & 0 \end{bmatrix} \\ \boldsymbol{D}_B &= \mathrm{diag}[L_1, L_2, C_1, C_2, C_B, C_{o1}] \\ x &= [x_1, x_2, x_3, x_4, x_5, x_6] \\ \boldsymbol{F} &= [0, 0, -1, \mu(t), 1-\mu(t), 0]^T i_2 \\ \boldsymbol{R}_B &= \mathrm{diag}[0, 0, 0, 0, 0, \tfrac{1}{R_{L1}}] \end{aligned} \tag{24}$$

where i_2 is the input current on the low-voltage side, $x_1 = \dot{q}_{L1}$, $x_2 = \dot{q}_{L2}$, $x_3 = q_{C1}/C_1$, $x_4 = q_{C2}/C_2$, $x_5 = q_{CB}/C_B$, and $x_6 = q_{Co1}/C_{o1}$.

The respective matrices in step-down mode are:

$$
\begin{aligned}
\boldsymbol{J}_B &= \begin{bmatrix} 0 & 0 & -1 & 1-\mu(t) & 0 & 0 \\ 0 & 0 & 0 & 1 & 1 & 0 \\ 1 & 0 & 0 & 0 & 0 & 0 \\ -[1-\mu(t)] & -1 & 0 & 0 & 0 & 0 \\ 0 & -1 & 0 & 0 & 0 & 0 \\ 0 & 0 & 0 & 0 & 0 & 0 \end{bmatrix} \\
\boldsymbol{D}_B &= \mathrm{diag}[L_1, L_2, C_1, C_2, C_B, C_{o2}] \\
x &= [x_1, x_2, x_3, x_4, x_5, x_6] \\
\boldsymbol{F} &= [0, 1, k, -[1-\mu(t)]k, -\mu(t)k, k]^T V_1 \\
\boldsymbol{R}_B &= \mathrm{diag}[0, 0, 0, 0, 0, \tfrac{1}{R_{L2}}]
\end{aligned} \tag{25}
$$

3.1. Design of the Passive Controller

Assuming the desired state variable is $\boldsymbol{x}_0$, the system error function is $\boldsymbol{x}_{\mathrm{e}} = \boldsymbol{x} - \boldsymbol{x}_0$. To make it converge quickly to the expectation, the damping factor $\boldsymbol{R}_a = \mathrm{diag}[R_a, R_a, R_a, R_a, R_a, 1/R_a]$ is introduced. Bringing it into Equation (23), the error equation is obtained as:

$$\boldsymbol{D}_B \cdot \dot{\boldsymbol{x}}_e + \boldsymbol{J}_B \cdot \boldsymbol{x}_e + (\boldsymbol{R}_B + \boldsymbol{R}_a) \cdot \boldsymbol{x}_e = \boldsymbol{F} - (\boldsymbol{D}_B \cdot \dot{\boldsymbol{x}}_0 + \boldsymbol{J}_B \cdot \boldsymbol{x}_0 + \boldsymbol{R}_B \cdot \boldsymbol{x}_0) + \boldsymbol{R}_a \boldsymbol{x}_e \tag{26}$$

Letting Equation (26) equal zero, the passive controller can be obtained as:

$$\boldsymbol{F} - (\boldsymbol{D}_B \cdot \dot{\boldsymbol{x}}_0 + \boldsymbol{J}_B \cdot \boldsymbol{x}_0 + \boldsymbol{R}_B \cdot \boldsymbol{x}_0) + \boldsymbol{R}_a \boldsymbol{x}_e = 0 \tag{27}$$

Define the switching function of the circuit's operating mode as:

$$\phi(t) = \begin{cases} 1 & t \in \text{when the converter operates in step} - \text{up mode} \\ 0 & t \in \text{when the converter operates in step} - \text{down mode} \end{cases} \tag{28}$$

Therefore, according to the first line of Equation (27), and combined with Equations (24) and (25), the passivity-based control law of the bidirectional high-gain Cuk circuit with basic gain network can be obtained as:

$$d(t) = \phi(t)[1 - \frac{2V_2}{V_1} - R_a \frac{x_1(t) - i_{L1}^*}{\frac{V_1}{2}}] + [1 - \phi(t)][\frac{2V_2}{V_1} - R_a \frac{x_1(t) - i_{L1}^*}{\frac{V_1}{2}}] \tag{29}$$

3.2. Design of LADRC

Auto-disturbance rejection control (ADRC) is a control technology that does not rely on the mathematical model of the controlled object. It can automatically detect and compensate the internal and external disturbances of the controlled object. The control object can acquire a good control effect when it encounters uncertain disturbance or parameter changes, and it has strong adaptability and robustness. However, there are many parameters of ADRC that have no physical significance. It is difficult to adjust. In view of this situation, linear ADRC is introduced in this paper, which not only has the advantages of good robustness of ADRC, but also avoids the disadvantages of many adjustable parameters, difficult adjustment, and large calculation.

Assuming that the devices of converters are all ideal, the input power of the bidirectional high-gain Cuk circuit with basic gain network is equal to the output power in step-up mode.

$$V_2 \cdot i_{L1}^* = V_1 \cdot (C_{o1} \frac{\mathrm{d}v_1}{\mathrm{d}t} + i_1) \tag{30}$$

Then, Equation (30) is organized into the standard form of active disturbance rejection control:

$$\frac{\mathrm{d}v_1}{\mathrm{d}t} = \frac{1}{C_{o1}} \cdot \frac{V_2}{V_1} \cdot i_{L1}^* + \frac{1}{C_{o1}} \cdot i_1 = b_o \cdot w + h \tag{31}$$

where $b_o = V_2/(C_{o1}V_1)$, $w = i_{L1}^*$, $h = i_1/C_{o1}$.

Since Equation (27) is a first-order equation, the first-order LADRC can be used to realize the control of voltage. Figure 7 shows the control block diagram of the passivity-based control with LADRC, where LESO is the first-order linear extended observer. LESO is used to eliminate unknown items and disturbances in the system. z_1 and z_2 are the outputs of the observer, $V_1{}^*$ is reference voltage on the high-voltage side, and $i_{L1}{}^*$ is reference current of the inductor L_1. The corresponding equations are as follows.

$$\begin{cases} \dot{z}_1 = z_2 + \beta_1(v_1 - z_1) + b_o y \\ \dot{z}_2 = \beta_2(v_1 - z_1) \end{cases} \tag{32}$$

The law of linear feedback control is:

$$\begin{cases} y = \frac{h_o - z_2}{b_o} \\ h_o = k_p(V_1^* - z_1) \end{cases} \tag{33}$$

Similarly, the first-order LADRC controller in step-down mode can be obtained. This is not repeated here, because its form is the same as step-up mode.

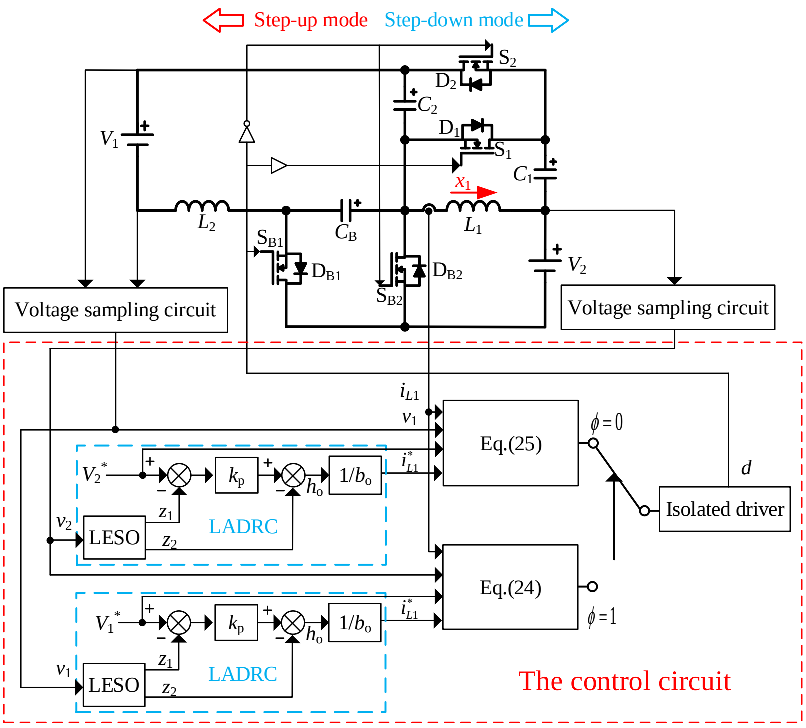

Figure 7. The passivity-based control with LADRC.

4. Results

4.1. Simulation Results

To verify the effectiveness of the proposed converter in this paper, a simulation model was built in Matlab/Simulink 2021(b). The simulation model parameters are V_2 = 48 V(36–60 V); V_1 = 400 V(300–450 V); P_o = 100 W; f_s = 50 kHz; L_1 = 1.2 mH; L_2 = 1.2 mH; C_1–C_4; C_B = 20 uF; and C_{o1}=100 uF.

4.1.1. Voltage and Current Waveform of Steady State

At steady state, the output voltage V_1 is set at 400 V in the step-up mode, and the voltage and current simulation waveform of the main device is shown in Figure 8, where v_{gs2} is the waveform of the drive signal; v_{SB2} is the voltage across S_{B2}; i_{SB2} is the current waveform flowing through S_{B2}; v_{C1}–v_{C2} and v_{CB} are the corresponding capacitor voltage waveforms; and v_{D1}–v_{D2} and v_{DB1} are the corresponding voltage waveforms across the diode.

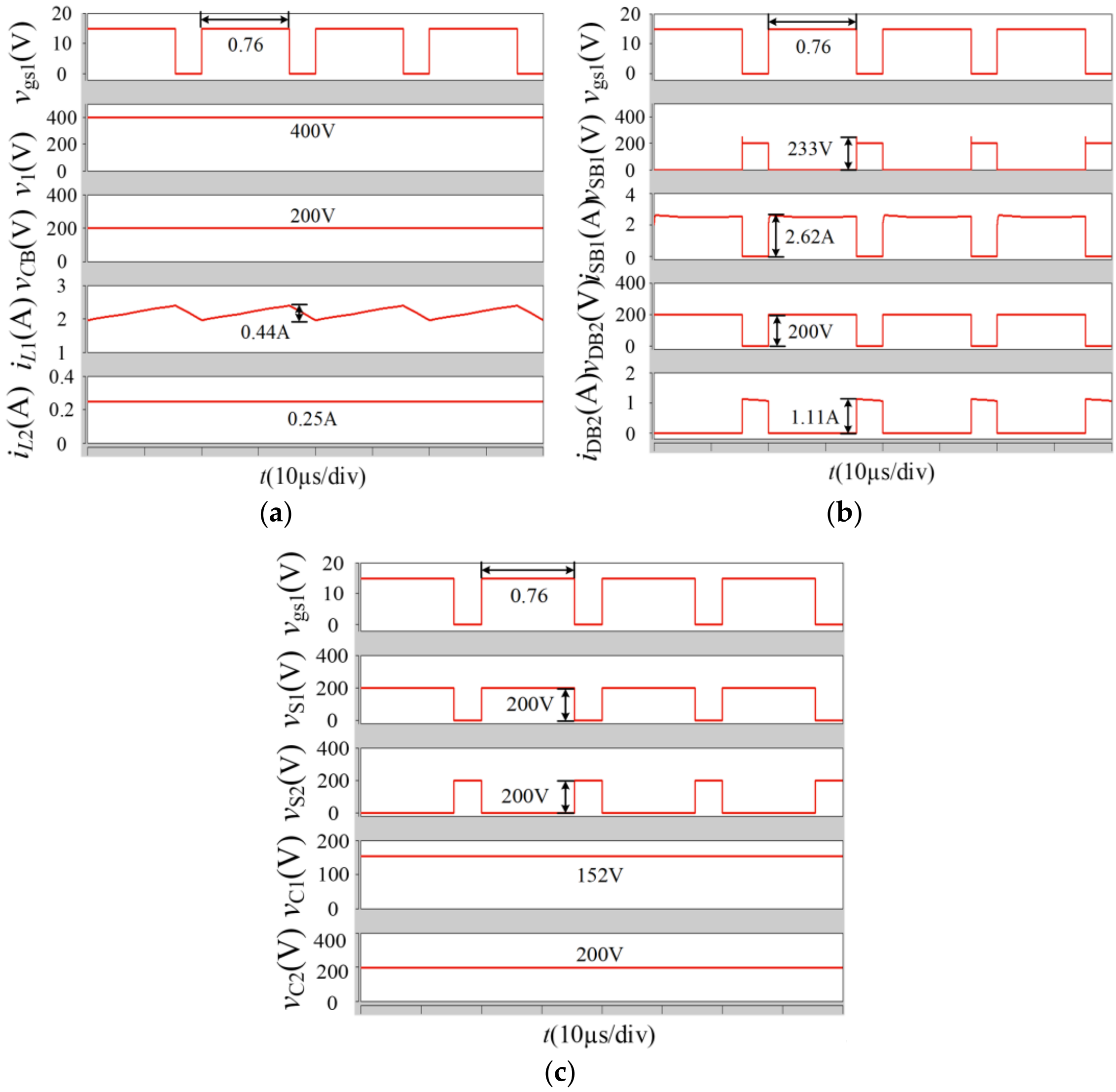

Figure 8. The steady waveforms in step-up mode (V_2 = 48 V): (**a**) v_{gs1}, v_1, v_{CB}, i_{L1}, i_{L2}; (**b**) v_{gs1}, v_{SB1}, i_{SB1}, v_{DB2}, i_{DB2}; (**c**) v_{gs1}, v_{S1}, v_{S2}, v_{C1} v_{C2}.

The output voltage V_2 is set at 48 V in the step-down mode, and the voltage and current simulation waveform of the main device are shown in Figure 9, where v_{gs1} and v_{gs2} are the waveforms of the drive signal; v_{SB1} is the voltage across S_{B1}; i_{SB1} is the current waveform flowing through S_{B1}; v_{C1}–v_{C2} and v_{CB} are the corresponding capacitor voltage waveforms; v_{S1}–v_{S2} is the voltage waveform of S_1, S_2; and v_{DB2} is the voltage waveform of D_{B2}.

With the above analysis, it can be seen that the simulation waveforms are consistent with the theoretical analysis, and the voltage stress of its semiconductor device is half of the voltage on the high-voltage side.

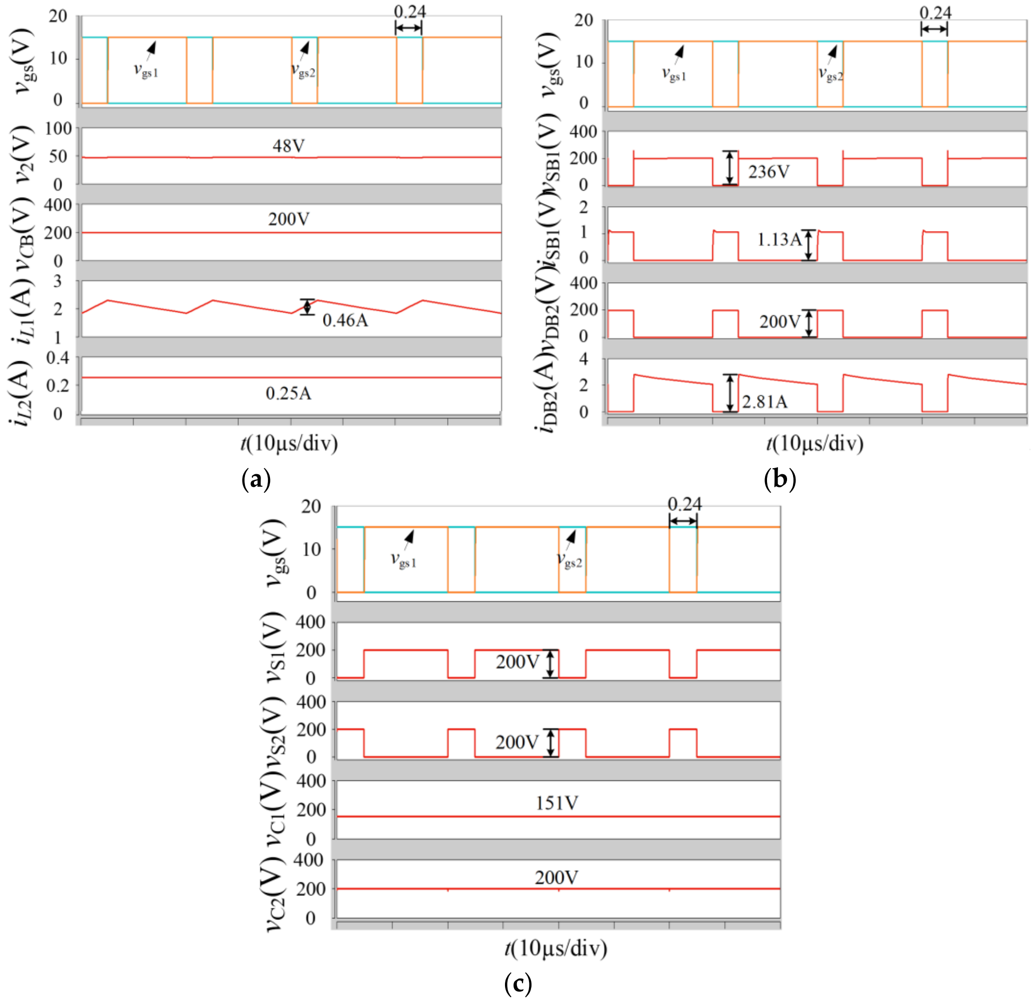

Figure 9. The steady waveforms in step-down mode (V_1 = 400 V): (**a**) v_{gs1}, v_{gs2}, v_2, v_{CB}, i_{L1}, i_{L2}; (**b**) v_{gs1}, v_{gs2}, v_{SB1}, i_{SB1}, v_{DB2}, i_{DB2}; (**c**) v_{gs1}, v_{gs2}, v_{S1}, v_{S2},v_{C1} v_{C2}.

4.1.2. Ripple Characteristics

In step-up mode, the simulation waveforms i_{L1} and i_{L2} of inductors L_1 and L_2 with different input voltages and different numbers of gain cells are shown in Figure 10. In step-down mode, these waveforms are shown in Figure 11. It is seen that the current waveform of i_{L2} is a straight line, after adding the gain unit. It achieves zero current ripple on the high-voltage side.

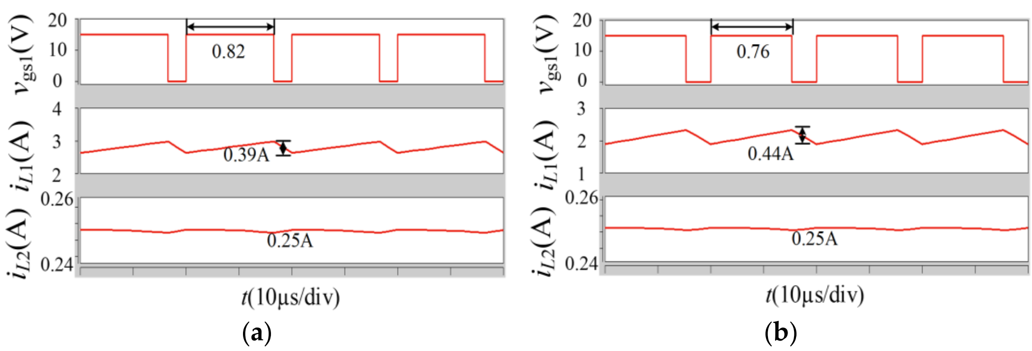

Figure 10. The stable simulation waveforms of i_{L1}, i_{L2} in step-up mode: (**a**) V_2 = 36 V; (**b**) V_2 = 48 V.

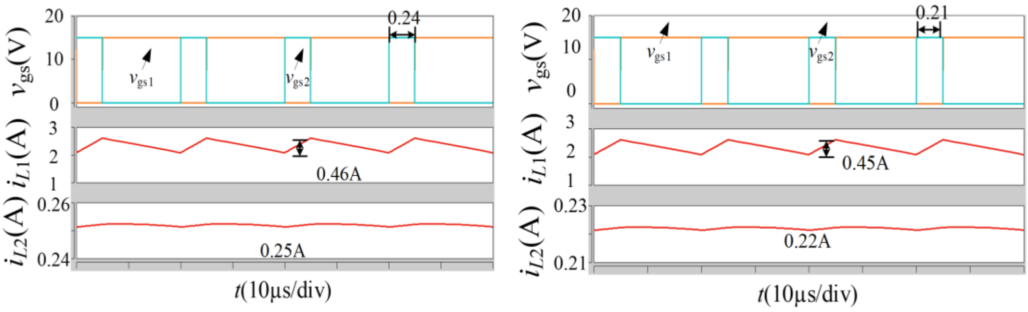

(**a**) (**b**)

Figure 11. The stable simulation waveforms of i_{L1}, i_{L2} in step-down mode: (**a**) V_1 = 400 V; (**b**) V_1 = 450 V.

4.1.3. Dynamic Characteristics

To verify the effectiveness of the proposed control strategy, the simulation of the passivity-based control with LADRC is carried out in this paper, and it is compared with the typical passivity-based control and the passivity-based control with PI.

In step-up mode, the variation in v_1 during the load step at V_2 = 48 V is shown in Figure 12. In step-down mode, the variation in v_2 during the load step at V_1 = 400 V is shown in Figure 13.

From Figures 12 and 13, it can be seen that when the power supply or load fluctuates, the output voltage of PBC has steady-state error, and the other two control output voltages have no error. In addition, when the power supply or load fluctuates, the output voltage overshoot of PBC is the largest, followed by PBC with PI, and the proposed control strategy is the smallest. Similarly, PBC control recovery time is the longest, followed by PBC with PI, and the proposed control strategy is the smallest.

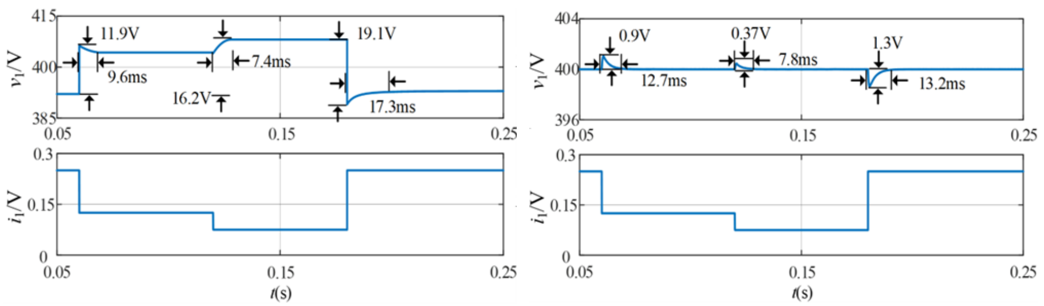

(**a**) (**b**)

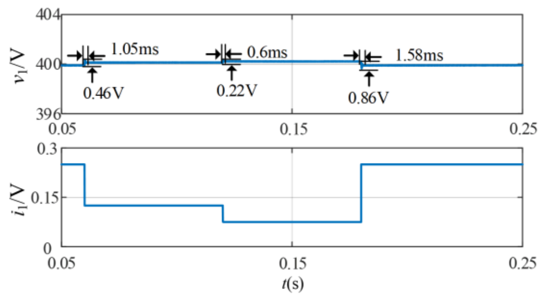

(**c**)

Figure 12. The dynamic waveforms of v_1 when i_1 changes in step-up mode: (**a**) PBC; (**b**) PBC with PI; (**c**) PBC with LADRC.

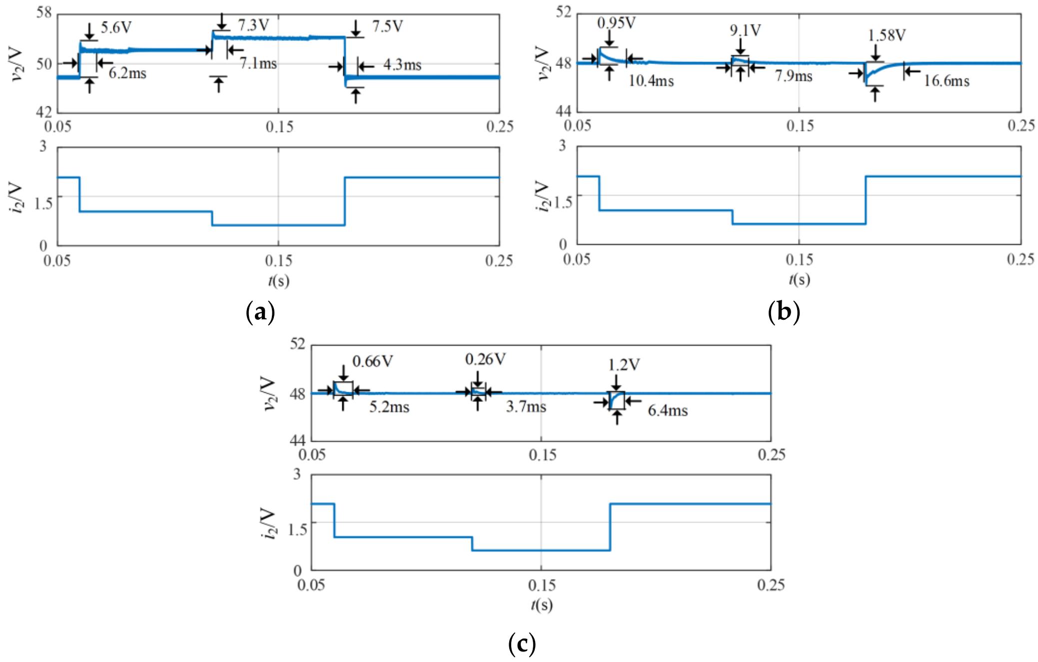

Figure 13. The dynamic waveforms of v_2 when i_2 changes in step-down mode: (**a**) PBC; (**b**) PBC with PI; (**c**) PBC with LADRC.

4.2. Experimental Results

A 100 W 48 V/400 V prototype was built to verify the validity of the theoretical analysis of the proposed converter. The prototype of the proposed converter is shown in Figure 14; the parameters of the experimental prototype are shown in Table 2.

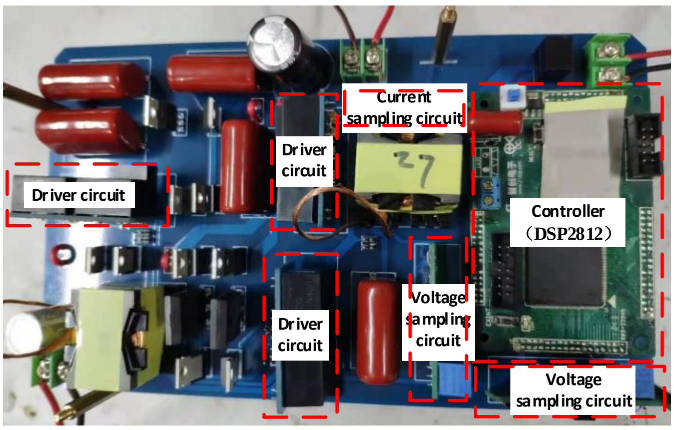

Figure 14. Prototype of the proposed converter.

Table 2. Parameters of an experimental prototype.

Parameters	Value	Parameters	Value
P_o/W	100	C_1–C_2	20 uF/630 V
V_1/V	400 (300–450)	C_B	20 uF/630 V
V_2/V	48 (36–60)	C_{o1}	100 uF/450 V
L_1/mH	1.2	C_{o2}	100 uF/160 V
L_2/mH	1.2	S_{B1}–S_{B2}	SVD12N65T
f_s/kHz	50	S_1–S_2	FCP099N65S3

4.2.1. Voltage and Current Waveform of Steady State

At V_2 = 48 V and P_o = 100 W, the steady-state waveform of the prototype in step-up mode is shown in Figure 15, where v_{SB2} is the voltage across S_{B2}; i_{SB2} is the current waveform flowing through S_{B2}; v_{C1}–v_{C2} and v_{CB} are the corresponding capacitor voltage waveforms; v_{D1}–v_{D2} and v_{DB1} are the corresponding voltage waveforms across the diode; and i_{L1} and i_{L2} are the current waveforms flowing through L_1 and L_2.

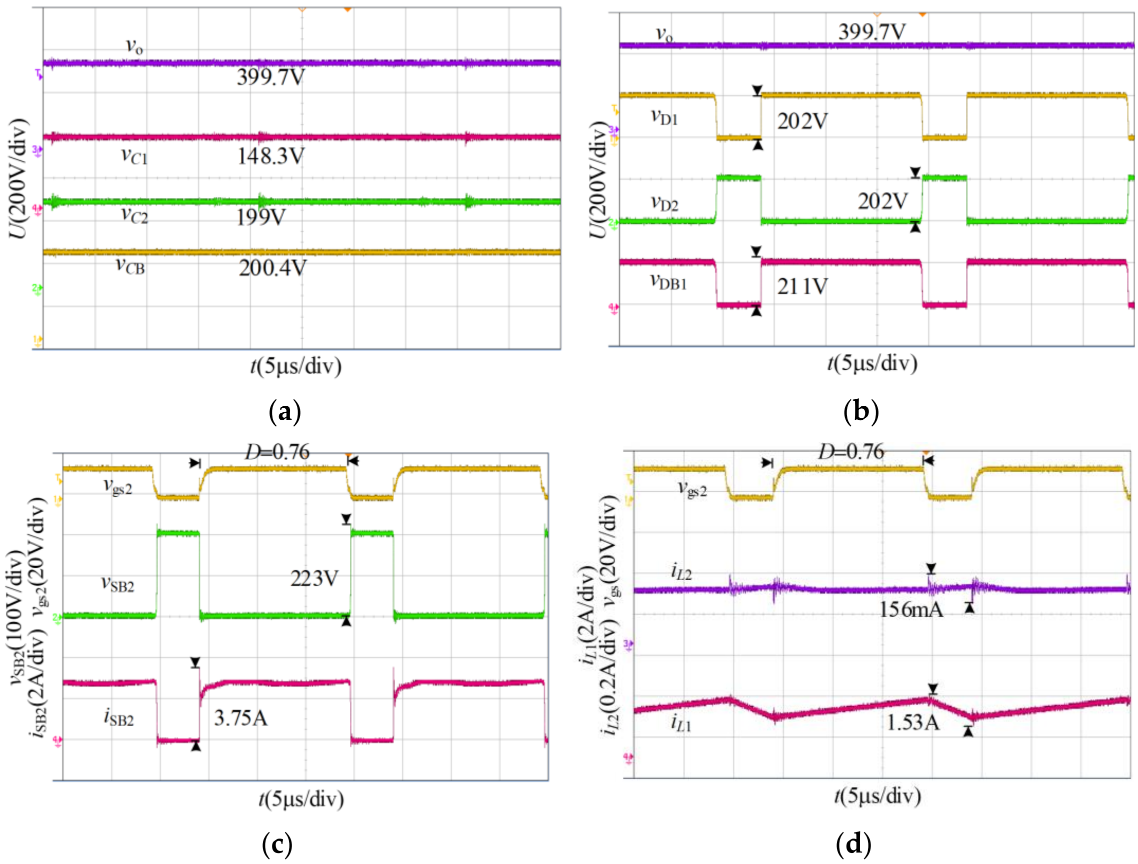

Figure 15. The steady waveforms of the proposed converter in step-up mode: (**a**) v_o, v_{C1}, v_{C2}, v_{CB}; (**b**) v_o, v_{D1}, v_{D2}, v_{DB1}; (**c**) v_{gs2}, v_{SB2}, i_{SB2}; (**d**) v_{gs2}, i_{L1}, i_{L2}.

At V_1 = 400V and P_o = 100 W, the steady-state waveform of the prototype in step-down mode is shown in Figure 16, where v_o is the output voltage; v_{gs1} and v_{gs2} are the waveforms of the drive signal; v_{SB1} is the voltage across S_{B1}; i_{SB1} is the current waveform flowing through S_{B1}; v_{C1}–v_{C2} and v_{CB} are the corresponding capacitor voltage waveforms; v_{S1}–v_{S2} is the corresponding voltage waveform across the switching, and v_{DB2} is the voltage waveform across D_{B2}; and i_{L1} and i_{L2} are the current waveforms flowing through L_1 and L_2.

As can be seen from Figure 15, the duty cycle of S_{B2} under the step-up mode is 0.76, and the output is stabilized to 399.7 V. The voltage stress of S_{B2} is 223 V, and the voltage stress of diodes D_1, D_2, and D_{B1} are 202, 202, and 211 V. Similarly, the duty cycle of S_{B1} under the step-down mode is 0.24, and the output is stabilized to 48.2 V, as shown in Figure 16. The corresponding voltage stresses of S_1, S_2, and S_{B1} are 208, 208, and 213 V, and the voltage stress of D_{B2} is 212 V.

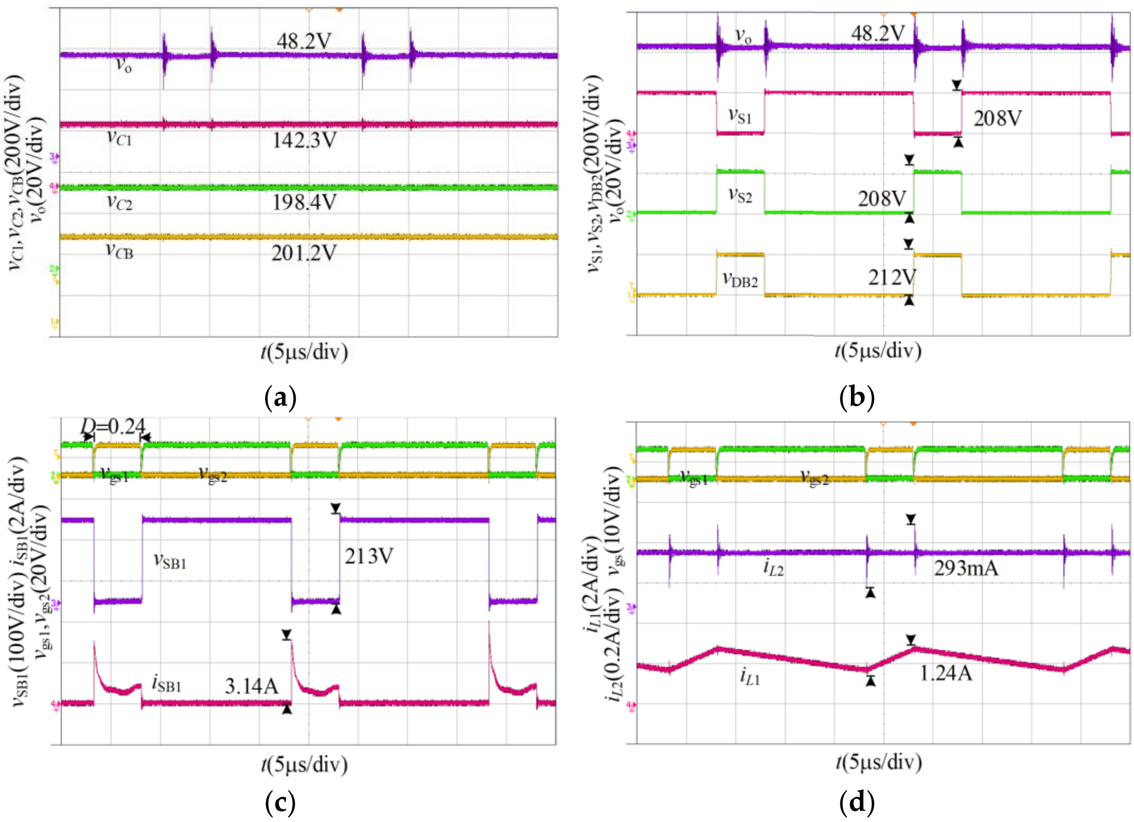

Figure 16. The steady waveforms of the proposed converter in step-down mode: (**a**) v_o, v_{C1}, v_{C2}, v_{CB}; (**b**) v_o, v_{S1}, v_{S2}, v_{DB2}; (**c**) v_{gs1}, v_{gs2}, v_{SB1}, i_{SB1}; (**d**) v_{gs1}, v_{gs2}, i_{L1}, i_{L2}.

4.2.2. Ripple Characteristics

In step-up mode, the stable experimental waveforms i_{L1} and i_{L2} of inductors L_1 and L_2 with different input voltages and different number of gain cells are shown in Figure 17. In step-down mode, these waveforms are shown in Figure 18. It is seen that the current waveform of i_{L2} is a straight line, after adding the gain unit. It achieves zero current ripple on the high-voltage side.

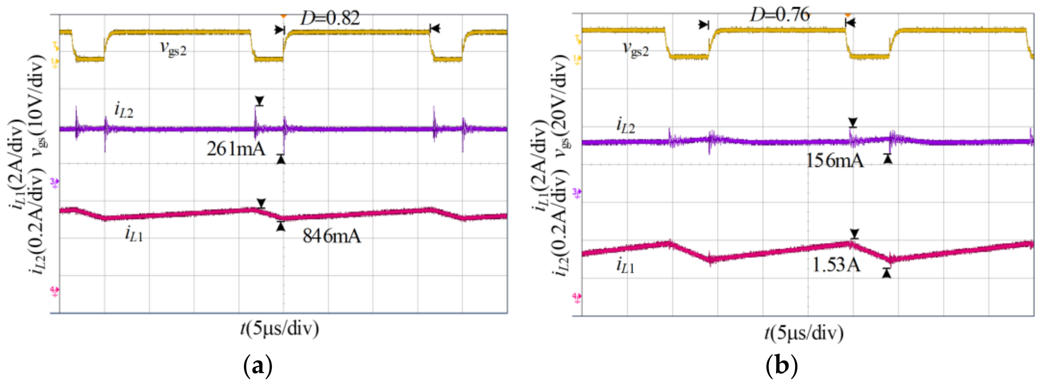

Figure 17. The stable experimental waveforms of i_{L1}, i_{L2} in step-up mode: (**a**) V_2 = 36 V; (**b**) V_2 = 48 V.

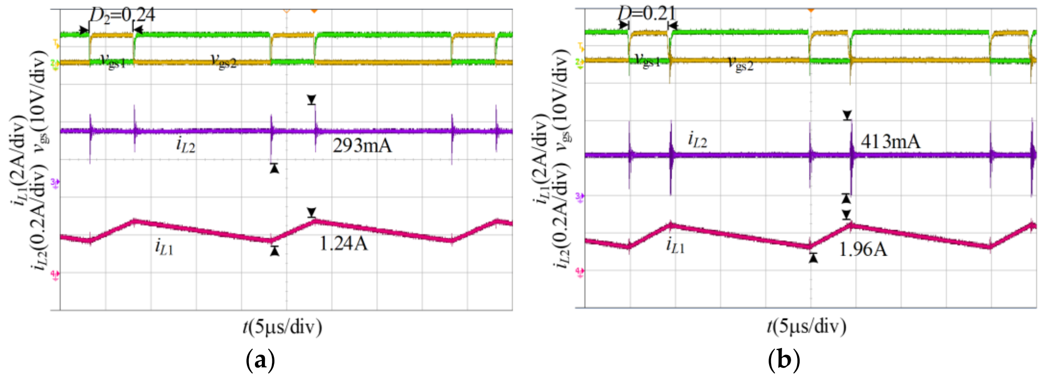

Figure 18. The stable experimental waveforms of i_{L1}, i_{L2} in step-down mode: (**a**) V_1 = 400 V; (**b**) V_1 = 450 V.

4.2.3. Efficiency Characteristics

The efficiency curves of the prototype operating in both directions are shown in Figure 19, where the horizontal coordinate is the output power P_o and the vertical coordinate is the efficiency η. As the number of cells increases, the efficiency of the proposed converter is higher.

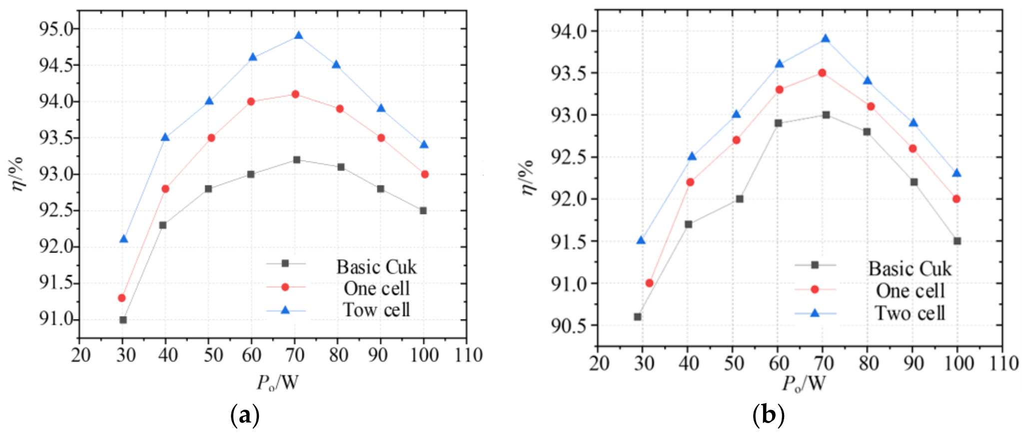

Figure 19. The efficiency curve of the prototype: (**a**) step-up mode; (**b**) step-down mode.

It can be seen from Figure 19 that the efficiency of the two units is the highest. Although the period increases with the increase in the number of units, the stress of the switch tube decreases significantly, and the total loss decreases.

4.2.4. Dynamic Characteristics

When v_2 jumps between 36 and 60 V, the dynamic response waveforms in step-up mode are shown in Figure 20. When v_2 varies in the ranges 36–48 V and 36–60 V, the data for dynamic performance are shown in Table 3.

Table 3. The dynamic performance comparison during the v_2 step in step-up mode.

	PBC		PBC with PI		PBC with LADRC	
Input voltage	Overshoot	Recovery time	Overshoot	Input voltage	Overshoot	Recovery time
36–48 V	6.83V	120 ms	4.75 V	86 ms	4.37 V	19 ms
48–36 V	−4.1V	154 ms	−1.94 V	80 ms	−1.38 V	40 ms
36–60 V	9.5V	192 ms	5.7 V	98 ms	4.74 V	46 ms
60–36 V	−5.5V	213 ms	−2.14 V	103 ms	−1.79 V	89 ms

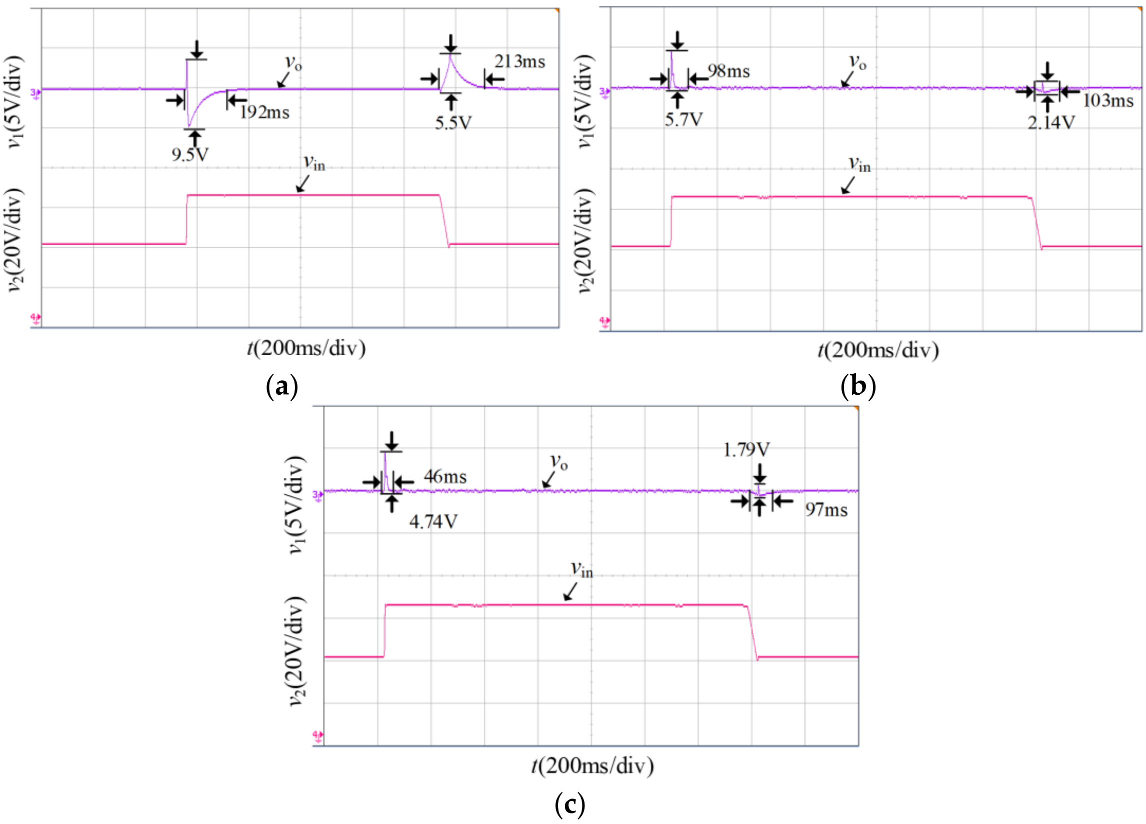

Figure 20. The dynamic response during v_2 step in step-up mode (36–60 V): (**a**) PBC; (**b**) PBC with PI; (**c**) PBC with LADRC.

When i_1 jumps between 0.08 and 0.25, the data for dynamic performance are shown in Table 4.

Table 4. The dynamic performance comparison during the v_2 step in step-up mode.

	PBC		**PBC with PI**		**PBC with LADRC**	
Input voltage	Overshoot	Recovery time	Overshoot	Input voltage	Overshoot	Recovery time
0.12–0.25 A	−2.31 V	39 ms	−2.34 V	87 ms	−1.04 V	19 ms
0.25–0.12 A	2.1 V	53 ms	2.41 V	83 ms	0.73 V	23 ms
0.08–0.25 A	−3.94 V	78 ms	−4 V	98 ms	−1.21 V	63 ms
0.25–0.08 A	3.69 V	84 ms	3.65 V	104 ms	0.94 V	72 ms

When v_1 jumps between 300 and 400 V, the dynamic response waveforms in step-down mode are shown in Figure 21. When v_1 varies in the ranges 300–400 and 400–450 V, the data for dynamic performance are shown in Table 5.

Table 5. The dynamic performance comparison during the v_2 step in step-down mode.

	PBC		**PBC with PI**		**PBC with LADRC**	
Input voltage	Overshoot	Recovery time	Overshoot	Recovery time	Overshoot	Recovery time
300–400 V	2.11 V	83 ms	2.23 V	56 ms	0.56 V	39 ms
400–300 V	−1.07 V	108 ms	−0.94 V	85 ms	−0.43 V	66 ms
400–450 V	2.11 V	83 ms	2.23 V	56 ms	0.56 V	39 ms
450–400 V	−1.07 V	108 ms	−0.94 V	85 ms	−0.43 V	66 ms

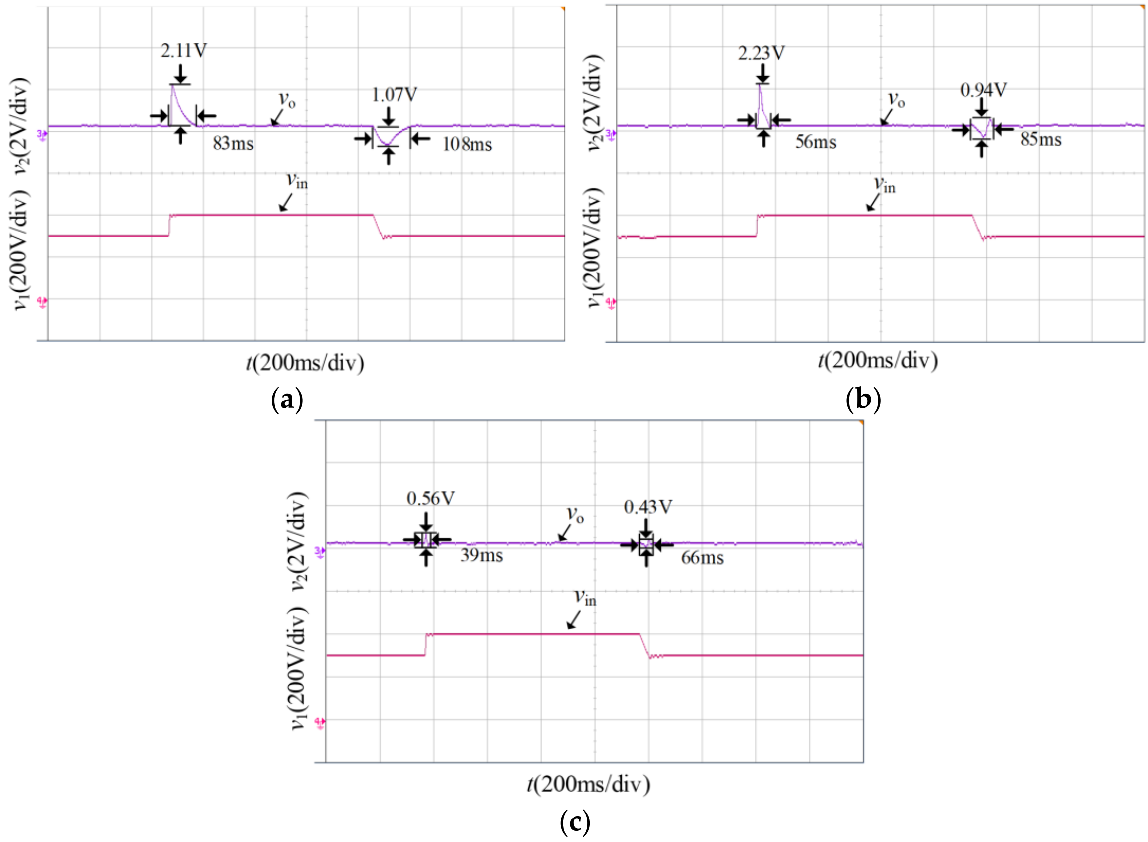

Figure 21. The dynamic response during v_1 step in step-down mode (300–400 V): (**a**) PBC; (**b**) PBC with PI; (**c**) PBC with LADRC.

For the changes in input voltage and output load, it can be seen from Figures 20 and 21 that the circuit has less voltage overshoot and shorter recovery time when applying the proposed control strategy described herein. Additionally, the proposed control strategy described in this paper demonstrates better performance in the dynamic process and achieves zero steady-state error.

When i_2 jumps between 0.63 and 2.08 A, the data for dynamic performance are shown in Table 6.

Table 6. The dynamic performance comparison during i_2 step in step-down mode.

	PBC		**PBC with PI**		**PBC with LADRC**	
Input voltage	Overshoot	Recovery time	Overshoot	Input voltage	Overshoot	Recovery time
1.04–2.08 A	−0.93 V	58 ms	−1.05 V	37 ms	−0.24 V	26 ms
2.08–1.04 A	0.72 V	66 ms	1 V	34 ms	0.31 V	29 ms
0.63–2.08 A	−2.17 V	75 ms	−2.08 V	54 ms	−0.62 V	38 ms
2.08–0.63 A	2.32 V	87 ms	1.81 V	53 ms	0.7 V	42 ms

5. Discussion

In this paper, progress is made in two aspects. First, a novel bidirectional converter topology is proposed. It has high voltage gain and low ripple. Compared with results reported in [23], it has higher efficiency. These advantages make it more suitable for application in a marine environment. Secondly, the proposed control strategy has strong adaptability and robustness. Compared with PBC or PBC with PI, it has better dynamic performance. It is very suitable for a marine environment because power supply or load is prone to large-range fluctuations. This paper achieves some results, but some aspects need further improvement: (1) Combine PBC with some intelligent optimization algorithms, such as neural network algorithm and genetic algorithm, to further improve the steady-state accuracy and dynamic performance of the control system. (2) Carry out engineering research for marine environment applications, such as waterproofing and anticorrosion. (3) Verifying the validity of bidirectional converter topology and its control strategy will be mainly completed in the laboratory. As a future research direction, we intend to direct this study to a practical case either carried out in situ or at one of the locations in the study.

6. Conclusions

Most deep-sea aquaculture industries heavily depend on transported fossil fuels. Thus, installing a distributed power generation system for these aquaculture industries is seen as very promising. A bidirectional DC–DC converter is essential for distributed power generation systems. It connects a variety of renewable energy sources with energy storage cells, and the DC bus voltage is usually high. The output voltage of batteries is usually low. Therefore, the high efficiency, low ripple, high voltage gain topology and its control robustness and stability of the converters will be the development trend, when it works in a marine environment. Thus, the zero-ripple bidirectional high-gain Cuk circuit proposed in the paper improves the voltage gain capability of the circuit by incorporating an extended switched-capacitor gain cell. This converter is characterized by simple structure, zero ripple, and low voltage stress of semiconductor power devices, and high voltage gain in both step-down and step-up modes. At the same time, passivity-based control with linear active disturbance rejection is proposed. This control strategy ensures that the system is stable when the power supply end or load end fluctuates in a large range. Additionally, it solves the problem of large steady-state errors that are caused by model errors and disturbances in the bidirectional high-gain converter that uses typical passivity-based control. The proposed control strategy solves the contradiction between rapidity and overshoot, which avoids the side effects of integral feedback. Compared with the PBC and PBC with PI, the proposed control strategy has better dynamic performance, such as smaller voltage overshoot and shorter recovery time. The simulation was carried out and a 100 W, 48 V/400 V prototype was built. The simulation and experimental results verify the validity of the theoretical analysis of the proposed circuit. The results show that the proposed control strategy has excellent control performance.

Author Contributions: Conceptualization, H.C. and W.L.; methodology, H.C. and W.L.; validation, H.C., W.L. and W.H.; formal analysis, H.C. and W.L.; investigation, H.C.; resources, W.L. and W.H.; data curation, H.C.; writing—original draft preparation, H.C.; writing—review and editing, W.L. and W.H.; visualization, H.C.; supervision, W.L. and W.H.; project administration, H.C. and W.L.; funding acquisition, H.C. and W.H. All authors have read and agreed to the published version of the manuscript.

Funding: This research was funded by the Fujian science and technology Major special project, grant number 2022NZ033023; the National Natural Science Foundation of China, grant number 52172327; special funds for marine economic development of Fujian Province, grant number FJHJF-L-2022-17; and the Education and Research Project for Young and Middle-aged Teachers of Fujian Provincial Department of Education, grant number JAT220317.

Institutional Review Board Statement: Not applicable.

Informed Consent Statement: Not applicable.

Data Availability Statement: Not applicable.

Conflicts of Interest: The authors declare no conflict of interest.

References

1. Onea, F.; Rusu, E. An Evaluation of Marine Renewable Energy Resources Complementarity in the Portuguese Nearshore. *J. Mar. Sci. Eng.* **2022**, *10*, 1901. [CrossRef]
2. Koričan, M.; Perčić, M.; Vladimir, N.; Alujević, N.; Fan, A. Alternative Power Options for Improvement of the Environmental Friendliness of Fishing Trawlers. *J. Mar. Sci. Eng.* **2022**, *10*, 1882. [CrossRef]
3. Taghavi, S.S.; Rezvanyvardom, M.; Mirzaei, A.; Gorji, S.A. High Step-Up Three-Level Soft Switching DC-DC Converter for Photovoltaic Generation Systems. *Energies* **2023**, *16*, 41. [CrossRef]
4. Liu, F.X.; Pan, Z.Z.; Ruan, X.B. Soft-Switching Analysis of a Boost-integrated Bidirectional Active Bridge DC/DC Converter. *Proc. CSEE* **2013**, *33*, 44–51.
5. Guo, H.W.; Wu, X.Z.; Wang, W. Novel Bidirectional Isolated DC/DC Converter Without Reactive Power Circulation. *Proc. CSEE* **2018**, *38*, 201–208.
6. Chengshan, W.; Zhen, W.; Peng, L. High efficiency power extraction control method for direct-drive linear wave energy converters based on forced resonance. *J. Trans. China Electrotech. Soc.* **2014**, *29*, 2624–2630.
7. Pires, V.F.; Foito, D.; Cordeiro, A. A DC-DC Converter with Quadratic Gain and Bidirectional Capability for Batteries/Supercapacitors. *IEEE Trans. Ind. Appl.* **2018**, *54*, 274–285. [CrossRef]
8. Zhang, H.; Chen, Y.; Shin, C.S.; Park, S.J.; Kim, D.H. Transformerless Bidirectional DC-DC Converter for Battery Storage System with High Voltage Gain. In Proceedings of the International Conference on Power Electronics and ECCE Asia, Busan, Republic of Korea, 27–30 May 2019.
9. Gunasekaran, D.; Qin, L.; Karki, U.; Li, Y.; Peng, F.Z. A Variable (n/m)X Switched Capacitor DC-DC Converter. *IEEE Trans. Power Electron.* **2017**, *32*, 6219–6235. [CrossRef]
10. Zhang, Y.; Gao, Y.P.; Zhou, L.; Sumner, M. A Switched-Capacitor Bidirectional DC-DC Converter With Wide Voltage Gain Range for Electric Vehicles With Hybrid Energy Sources. *IEEE Trans. Power Electron.* **2018**, *33*, 9459–9469. [CrossRef]
11. Hong, C.M.; Yang, L.S.; Liang, T.J.; Chen, J.F. Novel bidirectional DC-DC converter with high step-up/down voltage gain. In Proceedings of the 2009 Energy Conversion Congress and Exposition, San Jose, CA, USA, 20–24 September 2009.
12. Akhormeh, A.; Abbaszadeh, K.; Moradzadeh, M.; Shahirinia, A. High Gain Bidirectional Quadratic DC-DC Converter Based on Coupled Inductor with Current Ripple Reduction Capability. *IEEE Trans. Ind. Electron.* **2021**, *68*, 7826–7837. [CrossRef]
13. Zhang, Y.; Liu, Q.Q. Hybrid Switched Capacitor Switched Quasi-Z-Source Bidirectional DC–DC Converter With a Wide Voltage Gain Range for Hybrid Energy Sources EVs. *IEEE Trans. Ind. Electron.* **2019**, *66*, 2680–2690. [CrossRef]
14. Wu, L.T.; Yang, Z.H.; Xu, B.G. Investigation of Passivity-Based Control of DC-DC Converter. *Trans. China Electrotech. Soc.* **2004**, *19*, 66–69.
15. Cui, J.; Wang, J.H. Study of Passivity-Based Control of Buck Converter Based on Optimal Damping Injection. *J. Electr. Eng.* **2018**, *13*, 7–13.
16. Mihaly, V.; Susca, M.; Dobra, P. Passivity-Based Controller for Nonideal DC-to-DC Boost Converter. In Proceedings of the 2019 22nd International Conference on Control Systems and Computer Science (CSCS), Bucharest, Romania, 28–30 May 2019.
17. Hu, J.W.; Wang, J.H.; Tang, Q. Research on A New Type of High Gain Cuk Converter. *Trans. China Electrotech. Soc.* **2004**, *19*, 66–69.
18. Kim, T.W.; Park, S.K.; Ahn, H.H.; Yoon, S.S. Robust Passivity Based Control with Sliding Mode for DC-to-DC Converters. In Proceedings of the International Joint International on SICE-ICASE IEEE, Busan, Republic of Korea, 18–21 October 2006.
19. Hassan, M.A.; Li, E.P.; Li, X.; Duan, C.; Chi, S. Adaptive Passivity-Based Control of dc-dc Buck Power Converter With Constant Power Load in DC Microgrid Systems. *IEEE J. Emerg. Sel. Top. Power Electron.* **2019**, *7*, 2029–2040. [CrossRef]
20. Ortega, R.; Garcia-Canseco, E. Interconnection and damping assignment passivity-based control: A. survey. *Eur. J. Control* **2004**, *10*, 432–450. [CrossRef]
21. Gaviria, C.; Fossas, E.; Griñó, R. Robust controller for a full-bridge rectifier using the IDA approach and GSSA modeling. *IEEE Trans. Circuits Syst. I Reg. Pap.* **2005**, *52*, 609–616. [CrossRef]
22. Dòria-Cerezo, A. Modeling, simulation and control of doubly-fed induction machine controlled by back-to-back converter. Ph.D. Dissertation, Department Control Industrial System, Polytechnic University of Catalonia, Barcelona, Spain, 2006.
23. Cornea, O.; Andreescu, G.D.; Muntean, N.; Hulea, D. Bidirectional Power Flow Control in a DC Microgrid Through a Switched-Capacitor Cell Hybrid DC-DC Converter. *IEEE Trans. Ind. Electron.* **2017**, *64*, 3012–3022. [CrossRef]
24. Romeo, O.; Perez, L. Passivity-based Control of Euler Lagrange Systems. *Adapt. Disturb. Attenuation Frict. Compens.* **1998**, *26*, 75–92.
25. Chen, H.X. *Study on a High Gain Bidirectional DC-DC Cuk Converter and Its Nonlinear Control Strategy*; Fuzhou University: Fuzhou, China, 2021.